

## Article

# Comparative Study on the Evolution of Airflow Temperature and Valid Ventilation Distance Under Different Cooling Strategies in High-Temperature Tunnels for Mining Thermal Energy

Fangchao Kang <sup>1,2</sup> , Jinlong Men <sup>1,2</sup>, Binbin Qin <sup>1,2,3,4,\*</sup>, Guoxi Sun <sup>2,3,\*</sup>, Ruzhen Chen <sup>1</sup>, Weikang Zhang <sup>1</sup>, Jiamei Chen <sup>1</sup> and Zhenpeng Ye <sup>1</sup>

<sup>1</sup> School of Energy and Power Engineering, Guangdong University of Petrochemical Technology, Maoming 525000, China; fangchaokang@gdupt.edu.cn (F.K.); menjinlong@gdupt.edu.cn (J.M.); 0915crz@gdupt.edu.cn (R.C.); dg1309405778@gdupt.edu.cn (W.Z.); meiziqqq@gdupt.edu.cn (J.C.); yezhenpeng198@gdupt.edu.cn (Z.Y.)

<sup>2</sup> Guangdong Provincial Key Lab of Petrochemical Equipment Fault Diagnosis, Guangdong University of Petrochemical Technology, Maoming 525000, China

<sup>3</sup> Postdoctoral Innovation Practice Base, Guangdong University of Petrochemical Technology, Maoming 525000, China

<sup>4</sup> School of Automation Science and Engineering, South China University of Technology, Guangzhou 510640, China

\* Correspondence: qinbb611700@gdupt.edu.cn (B.Q.); guoxi.sun@gdupt.edu.cn (G.S.); Tel.: +86-13783915667 (B.Q.)

**Abstract:** A comprehensive understanding of airflow temperature distribution within high-temperature tunnels is crucial for developing effective cooling strategies that ensure a safe environment and acceptable construction costs. In this paper, we introduce a novel cooling strategy that integrates thermal insulation layers and heat exchangers aligned along the tunnel axis (TIL-HE strategy). We investigate variations in airflow temperature and valid ventilation distance (VVD) and compare them with two other cooling strategies: natural tunnels only employing mechanical ventilation (NT strategy) and tunnels featuring thermal insulation layers (TIL strategy), through the 3D k- $\epsilon$  turbulence model in COMSOL Multiphysics. Our findings indicate that (1) the TIL-HE strategy demonstrates superior cooling performance, resulting in significantly lower airflow temperatures and markedly higher VVD; (2) higher water velocity and more heat exchangers contribute to lower airflow temperature and prolonged VVD; (3) positioning the heat exchangers within the surrounding rock rather than inside the insulation layer leads to even lower airflow temperature and longer VVD. Longitudinal-arranged heat exchangers present fewer construction challenges compared to traditional radial-drilled ones, ultimately reducing tunnel construction costs. These findings provide valuable insights for optimizing cooling strategies and engineering parameters in high-temperature tunnel environments.

**Keywords:** thermal hazards; high-temperature tunnel; insulation layer; heat exchanger; valid ventilation distance



Academic Editor: Huaming Dai

Received: 28 November 2024

Revised: 18 December 2024

Accepted: 25 December 2024

Published: 3 January 2025

**Citation:** Kang, F.; Men, J.; Qin, B.; Sun, G.; Chen, R.; Zhang, W.; Chen, J.; Ye, Z. Comparative Study on the Evolution of Airflow Temperature and Valid Ventilation Distance Under Different Cooling Strategies in High-Temperature Tunnels for Mining Thermal Energy. *Fire* **2025**, *8*, 16. <https://doi.org/10.3390/fire8010016>

**Copyright:** © 2025 by the authors. Licensee MDPI, Basel, Switzerland. This article is an open access article distributed under the terms and conditions of the Creative Commons Attribution (CC BY) license (<https://creativecommons.org/licenses/by/4.0/>).

## 1. Introduction

Advancements in engineering technology have prompted humanity to embark on underground engineering projects in regions exhibiting increasingly intricate geological temperatures [1–3]. Tunnels with high geothermal temperatures are increasingly common, as evidenced by projects such as the Nige Tunnel (88 °C) [4], the Sangzhuling Tunnel (89 °C) [5,6], and the Sichuan-Tibet Railway Tunnel (208 °C) [7]. Notably, in the EGS-E

(enhanced geothermal systems based on excavation) (Figure 1) employed for mining HDR (hot dry rock) thermal energy, prolonged and extensive exposure to high-temperature surrounding rock poses a more significant challenge to preventing thermal hazards [8,9]. Such extreme temperature environments may shorten the lifespan of equipment and potentially pose health risks to personnel [10], compromising the safe excavation and operation of underground engineering projects [11]. Therefore, a thorough comprehension of the airflow temperature distribution within tunnels to propose effective insulation and cooling strategies is paramount for guaranteeing the long-term safety and operational sustainability of high-temperature tunnel projects [12,13].

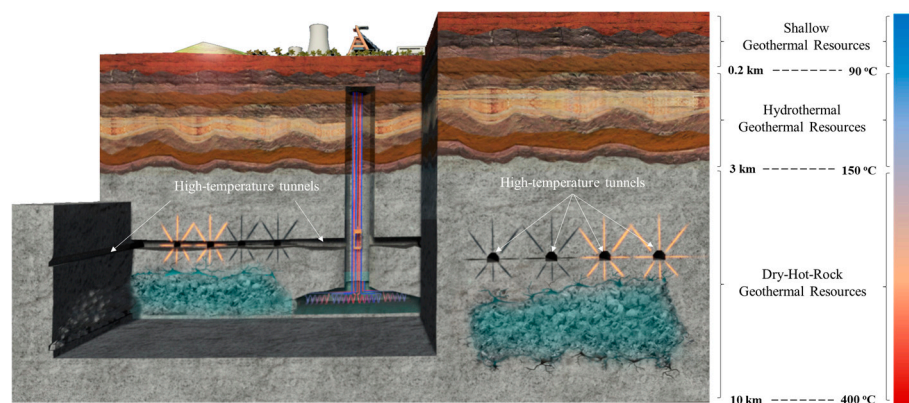


Figure 1. High-temperature tunnels in EGS-E.

The ambient temperature within a tunnel rapidly grows as the length of the excavated tunnel increases due to the temperature differences between the surrounding rock and the tunnel air [14]. Enhancing the heat removal capacity of the tunnel air through increasing ventilation velocity and reducing inlet temperature with a cooling system are acceptable ways to reduce such ambient temperatures [15,16]. Relevant studies mainly involve physical experiments and numerical models to propose reasonable airflow velocity and inlet temperature for special tunnels to reduce the cost of treating thermal hazards [13,17]. Installing an insulation layer increases thermal resistance and weakens heat transfer from the surrounding rock to the tunnel airflow for a safe ambient temperature [18,19]. The thermal insulation layer, whether laid on the surface of the surrounding rock or between the preliminary lining (Figure 2a) and the surrounding rock (Figure 2b), can prevent the tunnel from thermal damage [20,21]. Numerical simulation results indicate that the thermal insulation scheme can effectively reduce the temperature of the lining structure, thereby enhancing its thermal efficiency and performance [21]. Moreover, employing materials with lower thermal conductivity [22] and a thickening insulation layer [20] effectively decreases the airflow temperature, but presents exponentially increasing costs [23,24].

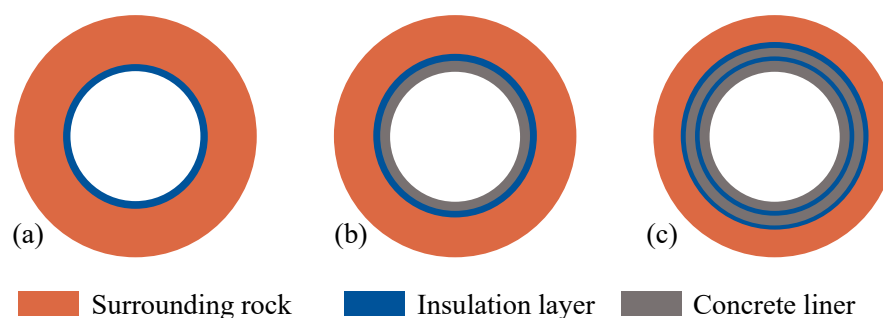
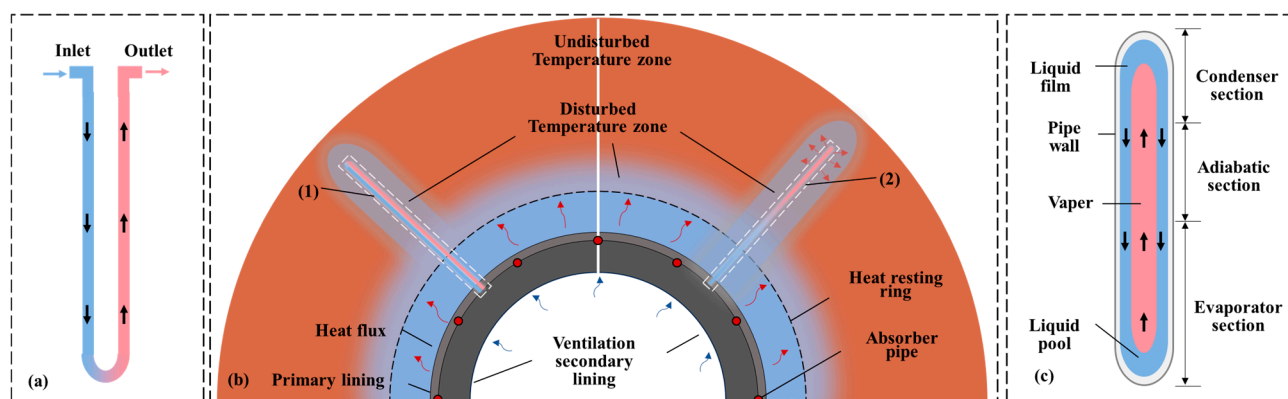


Figure 2. Lining and insulation layers with different schemes: (a) tunnel model with TIL, (b) tunnel model with TIL and concrete liner, and (c) tunnel model with multi-TIL.

Recent research has increasingly focused on modifying the structure of insulation layers. Examples include multi-layer insulation (Figure 2c) [21], corrugated insulation layers [25,26], and off-air insulation layers [26]. Double-layer insulation shows better cooling effects than single-layer insulation with the same total thickness [21], as well as changing the insulation layer from flat to corrugated [25,26]. An off-air insulation layer also enhances the cooling effect by adding an air layer with high thermal resistance between the insulation layer and the support layer [26]. However, such a cooling effect also rapidly decreases as the insulation layer thickens, which is unacceptable in ultra-high-temperature areas [27,28].

A combined cooling strategy incorporating insulation layers and heat exchangers demonstrates superior cooling performance in high-temperature tunnel environments. This strategy involves installing the insulation layers and heat exchangers radially within the surrounding rock at equal intervals using drilling technology. Various studies have primarily focused on the arrangement, location, and internal heat transfer medium of the heat exchangers, such as water pipelines (Figure 3a) [28] and thermosyphons (Figure 3b) [27]. Both systems significantly enhance cooling performance, albeit through different mechanisms. The former system transitions from low temperature to high-temperature water through conductive heat transfer between the surrounding rock and flowing water. Conversely, the latter operates based on phase change heat exchange, where high-temperature vapor undergoes gasification, subsequently cooling into low temperature liquid water.



**Figure 3.** Combined cooling strategies with insulation layers and heat exchangers. (a) is the enlarged view of (1); (b) is the combined cooling strategies; (c) is the enlarged view of (2) in (b).

In summary, significant progress has been made in tunnel air cooling, enabling ongoing projects in high-temperature tunnels. Notably, the combined cooling strategy effectively reduces airflow temperature and harvests thermal energy from the high-temperature water within the heat exchangers. However, existing heat exchangers remain complex structures with significant construction difficulties, posing considerable challenges to their widespread adoption. Additionally, the collaborative cooling mechanism between heat exchangers and insulation layers has not been thoroughly explored.

Here, we propose a novel cooling strategy that combines insulation layers with easy-to-build heat exchangers aligned along the tunnel axis (TIL-HE). Its cooling effectiveness is analyzed by employing a 3D  $k-\epsilon$  turbulence model in conjunction with solid–fluid convective heat transfer in COMSOL Multiphysics (version 6.0). We conduct a comparative analysis between the TIL-HE strategy and two other strategies: natural tunnels without a thermal insulation layer (NT), and tunnels with a thermal insulation layer (TIL), focusing on the alterations in airflow temperatures and associated valid ventilation distance (VVD). Additionally, a sensitivity analysis of the TIL-HE strategy is performed by altering the heat

exchanger configuration, water flow velocity, and installation position, which may yield valuable insights into optimizing cooling strategies in high-temperature tunnels.

## 2. Materials and Methods

### 2.1. Fundamental Assumptions

We adopted several basal simplifications and assumptions to enhance the convergence of turbulent flow calculations and facilitate computation and analysis [14,29,30]: (1) the physical properties of surrounding rock, pipes, and insulation layers are constant, uniform, and isotropically thermal; (2) the airflow in tunnels and the water in pipes are weakly compressible; (3) the thermal radiation among tunnel walls is not considered, as well as among pipe walls; (4) heat dissipation from the surrounding rocks and heat dissipation caused by fluid viscosity were not considered; (5) the influence of pressure on airflow density and temperature, moisture evaporation, and the humidity and mass exchanges within the tunnel is inconsiderable; (6) effective thermal contact exists between each layer, with negligible thermal resistance.

### 2.2. Governing Equations

Heat transfer within the tunnel consists of heat conduction and heat convection. Heat conduction occurs in the surrounding rock, insulation layer, and heat exchanger, while heat convection primarily occurs between the airflow and tunnel wall, as well as the water and the pipe wall. When heat exchange occurs mainly in the form of heat convection within the tunnel, insulation layer, and heat exchanger, the equation is as follows:

$$\rho c_p \frac{\partial T}{\partial t} + \nabla \cdot \mathbf{q} = Q \quad (1)$$

$$\mathbf{q} = -k \nabla T \quad (2)$$

where  $\rho$  is the density of the surrounding rock, insulation layer, and heat exchanger;  $c_p$  is the specific heat capacity at constant pressure;  $T$  is the temperature;  $t$  is time;  $\mathbf{q}$  is the heat flux density;  $Q$  is the heat source; and  $k$  is the thermal conductivity.

The temperature field in the tunnel experiences temporal variations, signifying a non-steady state condition during tunnel excavation. Thus, we employed the Reynolds-averaged Navier–Stokes (RANS) equations, a well-established approach in fluid mechanics for turbulence description with reliable results, to describe turbulent fluid within the tunnel exhibiting non-isothermal flow characteristics. The pertinent governing equations encompass the momentum equation (N-S equation), time-averaged mass equation,  $k$ - $\varepsilon$  two-equation turbulence model, and energy equation, as presented below [31,32]:

(1) Momentum conservation (Navier–Stokes equation)

$$\rho_a \frac{\partial \mathbf{u}}{\partial t} + \rho_a (\mathbf{u}_a \cdot \nabla) \mathbf{u}_a = \nabla \cdot [-p\mathbf{I} + \mathbf{K}] + \mathbf{F} \quad (3)$$

$$\mathbf{K} = (\mu + \mu_T) \left( \nabla \mathbf{u}_a + (\nabla \mathbf{u}_a)^T \right) - \frac{2}{3} (\mu + \mu_T) (\nabla \cdot \mathbf{u}_a) \mathbf{I} - \frac{2}{3} \rho_a k \mathbf{I} \quad (4)$$

where  $\mu$ ,  $\mu_T$ , and  $\mathbf{I}$  are the viscosity coefficient, dynamic viscosity, and characteristic matrix of the air and water flow, respectively. Regarding the second viscosity coefficient of airflow:  $\mu' = 2/3\mu(\nabla \cdot \mathbf{u}_a)$ ;  $\mathbf{F} = \rho_a \mathbf{X} - \partial/\partial x(\mu' \nabla \cdot \mathbf{u}_a)$ , where  $\mathbf{X}$  is the force along the axis.

(2) Mass conservation equation

$$\frac{\partial \rho_a}{\partial t} + \nabla \cdot (\rho_a \mathbf{u}_a) = 0 \quad (5)$$

$$\rho_a = \rho_a(p, T_a) \tag{6}$$

where  $\rho_a$ ,  $u_a$ ,  $p$ , and  $T_a$  are the density, velocity, pressure, and temperature of the airflow and water, respectively.

(3)  $k$ - $\varepsilon$  turbulence model

$$\rho_a \frac{\partial k}{\partial t} + \rho_a (\mathbf{u}_a \cdot \nabla) k = \nabla \cdot \left[ \left( \mu + \frac{\mu_T}{\sigma_k} \right) \nabla k \right] + p_k - \rho_a \zeta \tag{7}$$

$$\rho_a \frac{\partial \zeta}{\partial t} + \rho_a (\mathbf{u}_a \cdot \nabla) \zeta = \nabla \cdot \left[ \left( \mu + \frac{\mu_T}{\sigma_\varepsilon} \right) \nabla \zeta \right] + C_{\zeta 1} \frac{\zeta}{k} p_k - C_{\zeta 2} \rho_a \frac{\zeta^2}{k} \tag{8}$$

where  $k$  and  $\varepsilon$  are the turbulent kinetic energy and its dissipation rate of the airflow and water, respectively.  $p_k = \mu_T \left[ \nabla \mathbf{u}_a : \left( \nabla \mathbf{u}_a + (\nabla \mathbf{u}_a)^T \right) \right] - 2/3 (\nabla \cdot \mathbf{u})^2 - 2/3 \rho_a k \nabla \cdot \mathbf{u}_a$ ;  $\mu_T = \rho_a C_\mu k^2 / \zeta$ ;  $C_{\zeta 1}$ ,  $C_{\zeta 2}$ ,  $C_\mu$ ,  $\sigma_\zeta$ , and  $\sigma_k$  are empirical constants determined based on previous studies [33].

(4) Energy conservation equation

$$\rho_a C_{pa} \frac{\partial T_a}{\partial t} + \rho_a C_{pa} \mathbf{u}_a \nabla T_a + \nabla \cdot \mathbf{q}_a = Q \tag{9}$$

$$\mathbf{q}_a = -\lambda_a \nabla T_a \tag{10}$$

where  $C_{pa}$  is the specific heat capacity of the airflow and water;  $\mathbf{q}_a$  is the heat flux density;  $\lambda_a$  is the variable thermal conductivity concerning  $T_a$ ; and  $Q$  is their heat source.

2.3. Numerical Model and Boundary Conditions

2.3.1. Engineering Requirements

Dealing with high-temperature rock is an unavoidable challenge when exploiting deep underground resources [34,35], during which manually solving intricate heat conduction partial differential equations can be particularly challenging in the analysis of complex fluid dynamics, thermal dynamics, and related fields. Numerical simulation software, such as COMSOL Multiphysics [36], has become acceptable for simulating and analyzing temperature variations in high-temperature tunnels [8,37–39]. We validate the results of Blay’s laboratory experiments [39,40], through the same model in COMSOL Multiphysics (version 6.0), as shown in Figure 4a. The numerical curves agree well with the experiment data (Figure 4b). Thus, COMSOL Multiphysics is capable of predicting airflow temperature distribution variation.

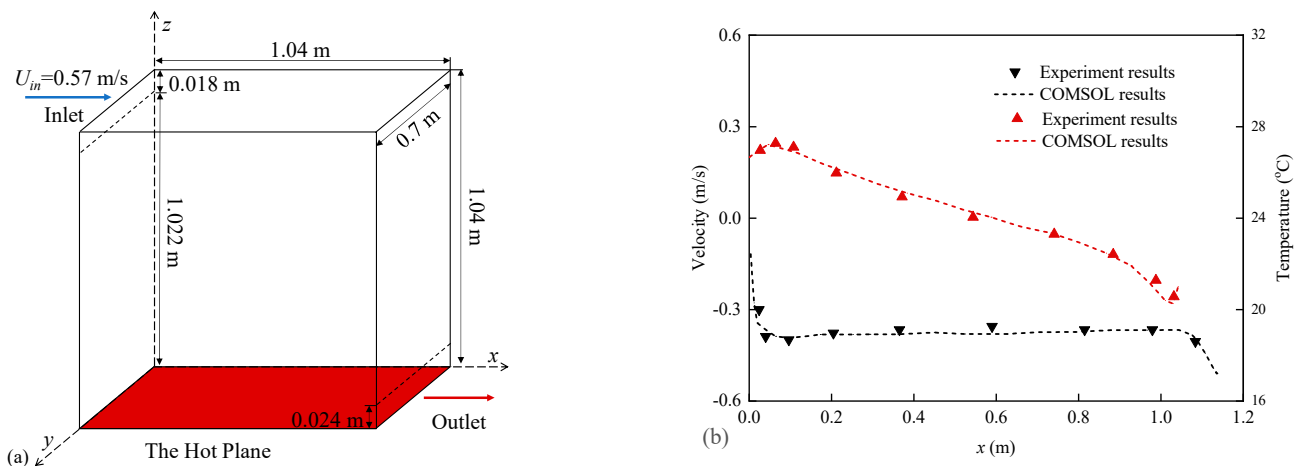
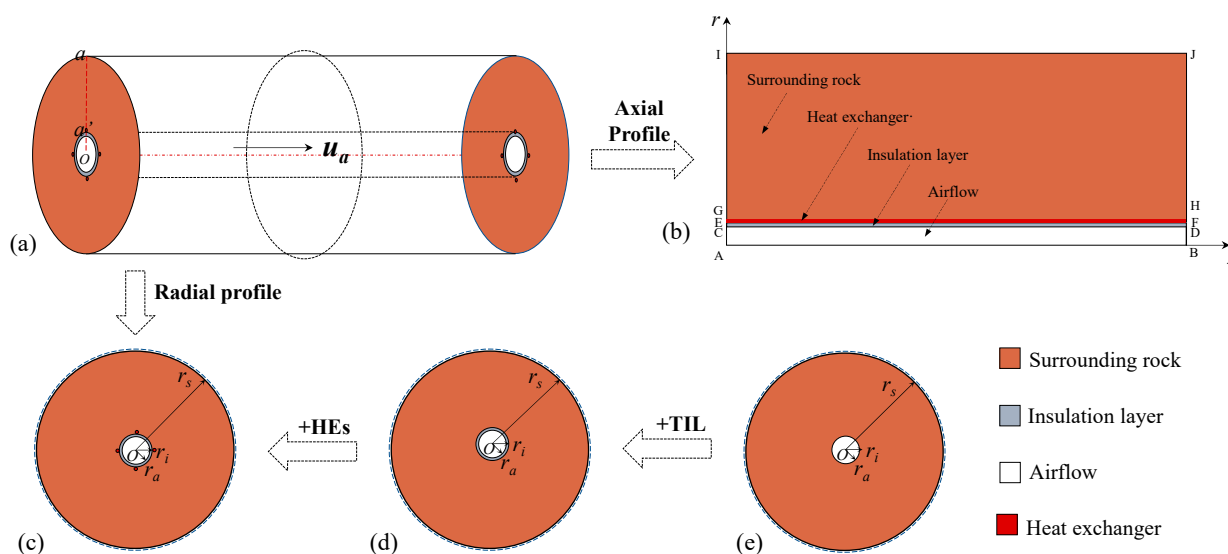


Figure 4. Comparison of experimental and numerical simulation results: (a) experimental schematic diagram; (b) temperature and velocity distribution at mid-width.

### 2.3.2. Numerical Models

The numerical model in this paper encompasses various layers, including the surrounding rock, insulation layer, heat exchanger, water flow, and airflow, necessitating examining heat transfer between solid and fluid components. We built a 3D cylindrical tunnel model (Figure 5a,b) with a hollow geometric shape lining the insulation layer and heat exchanger to investigate the temperature variation in the airflow under three different cooling strategies. Figure 5c shows the tunnel cross-section of the TIL-HE model, which employs a composite structure consisting of insulation layers and heat exchangers aligned along the tunnel axis. In this model, flow circulation is implemented by applying a constant injection rate of airflow ( $u_a$ ) that flows through the tunnel from the left end (AC) to the right end (BD). Thermal insulation is imposed on the left end (AI), top end (IJ), and right end (BJ). The heat is transferred vertically from the surrounding rock to the heat exchanger, then to the TIL boundary and airflow.



**Figure 5.** Diagram of numerical models of different cooling strategies: (a) 3D cylindrical tunnel model, (b) 2D section of tunnel model along ventilation direction, (c) 2D radial section of TIL-HE model, (d) 2D radial section of TIL model, and (e) 2D radial section of NT model.

Figure 5d is the tunnel cross-section of the TIL model lined with a thermal insulation layer on the tunnel surface; Figure 5e presents the NT model, only with mechanical ventilation for tunnel cooling without a thermal insulation layer. The length of the tunnel model is 1000 m; the thickness of the TIL and surrounding rock are 0.1 m and 100 m, respectively; and the radii of the tunnel and heat exchanger are 0.05 m and 2.75 m, respectively. The mesh volume of the TIL-HE model is  $2.82 \times 10^6 \text{ m}^3$ , comprised of tetrahedra, prism, triangle, and quadrilateral elements, where its total element number, minimum element quality, average element quality, and element volume ratio are 5,978,691,  $3.81 \times 10^{-4}$ , 0.60, and  $1.02 \times 10^{-8}$ , respectively. The thermophysical parameters of the surrounding rock, insulation layer, heat exchanger, airflow, and water are detailed in Table 1.

**Table 1.** Thermophysical parameters of the high-temperature roadway model.

Layers	Thermal Conductivity (W/(m·K))	Density (kg/m <sup>3</sup> )	Heat Capacity (J/(kg·K))
Surrounding rock	2.4	2600	850
TIL	0.1	500	500
Heat exchanger	21.5	7930	518

### 2.3.3. Boundary and Initial Conditions

The boundary and initial conditions are defined as follows:

- (1) The airflow enters the tunnel from the inlet with a velocity of  $u_a = -u_0n$  and exits through the outlet with following conditions:  $-n \cdot q = 0$  and  $p = p_{atm}$ . The water flows in the heat exchanger inlet with a velocity of  $u_w = -u_1n$  and exits through the pipe outlet with the same conditions as the airflow.
- (2) Heat exchange between the surrounding rock and the airflow is governed by the heat flux boundary:  $-n \cdot q = h(T_r - T_a)$ . We employed a wall function to calculate the convective heat transfer coefficient of the airflow for improving computational accuracy using the following formula:

$$h = \frac{c_{pa}\rho_a C_\mu^{0.25} k_a^{0.5}}{T^+} \tag{11}$$

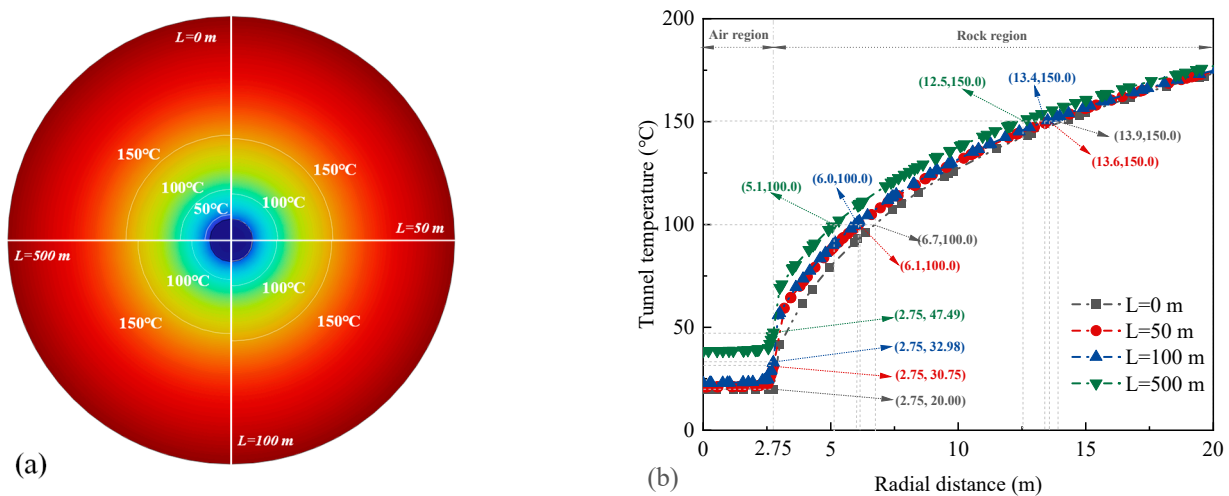
where  $T^+$  is the dimensionless temperature in COMSOL Multiphysics, expressed using the dimensionless wall function ( $y^+$ ), where  $T^+ = T^+(y^+)$ .

- (3) The outer boundary is set as a constant temperature, with a value equal to the initial temperature of the surrounding rock.
- (4) Due to a sufficiently wide computational domain in the model, the radial boundaries of the surrounding rock and the airflow and water flow outlets are considered adiabatic.
- (5) The initial conditions of the model are as follows: the temperature of the surrounding rock is  $T_r = 200$  °C, the temperature of the airflow is  $T_a = 20$  °C, the velocity of the airflow is  $u_a = 1$  m/s, and the velocity of the water flow is  $u_w = 0.2$  m/s.

## 3. Results and Analysis

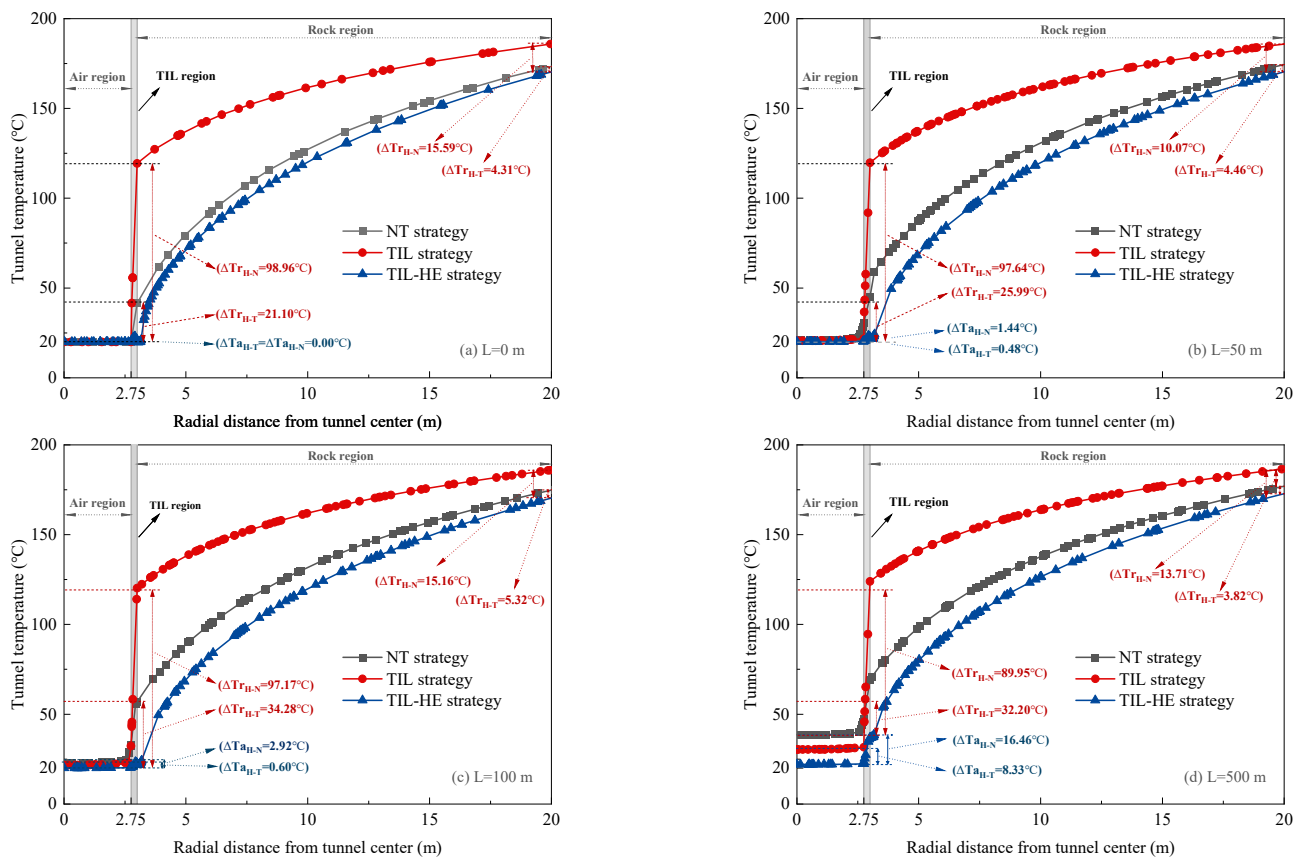
### 3.1. Radial Temperature Variation in the High-Temperature Tunnel

Figure 6 illustrates the radial temperature distribution at different ventilation distances ( $L$ ) in the high-temperature tunnel. At the tunnel entrance ( $L = 0$  m), the airflow temperature stays at the initial state of 20 °C, where the rock temperature gradually increases from the tunnel wall to the interior rock. The tunnel temperature ascends from the tunnel center to the tunnel wall as the ventilation distance grows, resulting in a tunnel center temperature of 38.51 °C and a tunnel center temperature of 47.49 °C when the ventilation distance reaches 500 m. Such a temperature has exceeded the safety standard of the tunnel air temperature, requiring mandatory cooling measures to decrease it [8].



**Figure 6.** Temperature distribution at different ventilation distances under the NT strategy: (a) radial temperature nephogram under different  $L$  and (b) radial temperature comparison under different  $L$ .

Figure 7 compares the different temperature evolutions in the high-temperature tunnel under three different cooling strategies. The tunnel temperature under the TIL strategy presents a gradual decrease in the air region and a sharp increase in the rock region compared to that without TIL, whereas the tunnel with TIL-HE presents a further decrease in both regions. The difference in the air temperature under different strategies is negligible at the tunnel entrance (Figure 7a,b), gradually becoming noticeable as the ventilation distance grows (Figure 7c,d). The center air temperature in the tunnel with TIL-HE is 0.48 °C lower than that with TIL and 1.44 °C than that without TIL at  $L = 50$  m (Figure 7b), which grows to 8.33 °C and 16.46 °C at  $L = 500$  m (Figure 7d), respectively. The rock temperature under TIL-HE strategy is lowest, presenting a difference of 21.10 °C compared to the NT tunnel and a difference of 98.96 °C compared to the TIL tunnel at the entrance (Figure 7a). These differences decrease with the increased ventilation distances, which decrease to 97.17 °C and 34.28 °C, respectively, at  $L = 100$  m (Figure 7c). Meanwhile, this rock temperature difference among three cooling strategies gradually reduces along the tunnel wall to the interior when the ventilation distance remains unchanged. The wall temperature of the tunnel with TIL-HE is lower, at 89.95 °C, than that with TIL, which decreases to 13.71 °C when  $R = 20$  m (Figure 7d).



**Figure 7.** Temperature evolution along the radial direction under different strategies: (a) tunnel temperature at  $L = 0$  m, (b) tunnel temperature at  $L = 50$  m, (c) tunnel temperature at  $L = 100$  m, and (d) tunnel temperature at  $L = 500$  m.

Meanwhile, the TIL temperature jumps from the inner boundary to the outer in the TIL tunnel, increasing from 20 °C to 119.37 °C at the entrance (Figure 7a). This dramatic increase gradually weakens as the ventilated distance increases, decreasing from 99.37 °C at  $L = 0$  m to 92.37 °C at  $L = 500$  m (Figure 7d). The difference between the inner boundary and the outer in the TIL-HE tunnel is not obvious, at the entrance with an increase of

0.05 °C (Figure 7a), which becomes pronounced as the ventilated distance increases, rising to an increase of 11.44 °C (Figure 7d).

### 3.2. Air Temperature Evolution Along the Ventilation Direction

Figure 8 illustrates the airflow temperature distribution of the tunnel center and wall, exhibiting the noticeable difference in temperature variation among the three cooling strategies. Although the air temperature increases as the ventilation distance grows under the different cooling strategies, significant variations are observed in the temperature increase. The NT tunnel exhibits the highest increase, followed by the TIL tunnel, while the TIL-HE tunnel shows the lowest.

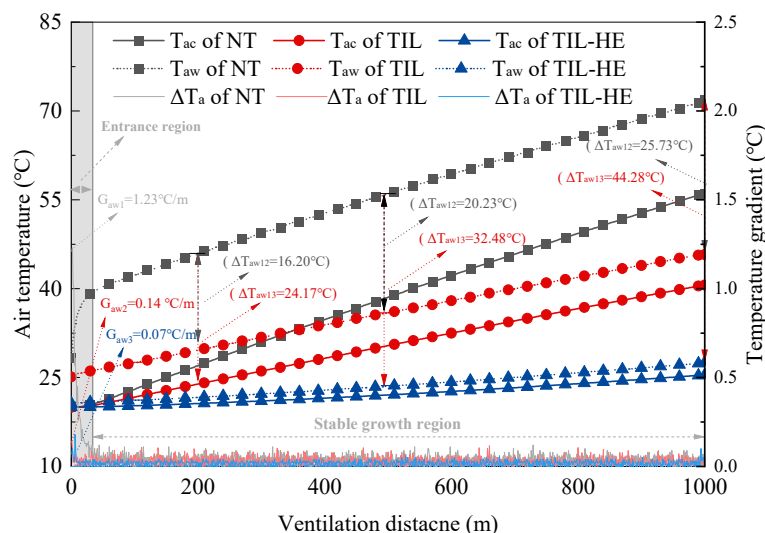


Figure 8. Evolution in temperature and associated temperature difference under three strategies.

Two distinct regions are exhibited along the ventilation direction: the entrance and stable growth regions, with the temperature growth rate in the former sharper than that in the latter. The wall temperature shows a markable increase in the former and a stable growth in the latter, whereas the center temperature remains unchanged in the former and increases at a stable rate in the latter. That is consistent with our previous research [8], in which a longer ventilation distance was used. Moreover, the difference in temperature in the entrance region is negligible in the TIL and TIL-HE tunnels.

With the installation of heat exchangers, the overall wall temperature in the tunnel decreases, leading to a gradual reduction in heat exchange between the tunnel wall and the tunnel air. The wall temperature growth rate of the NT tunnel is 1.23 °C/m at  $L = 1$  m, which drops to 0.06 °C/m at  $L = 50$  m, then presents an insignificant fluctuation from  $L = 50$  m to  $L = 1000$  m. The temperature increases along the ventilation direction in the TIL and TIL-HE tunnels are lower than those in the NT tunnel, showing 0.14 °C/m and 0.07 °C/m of the wall temperature growth rates at  $L = 1$  m, respectively. The average wall temperature growth rate also decreases to 0.02 °C/m and 0.01 °C/m in the TIL and TIL-HE tunnels.

The difference in the temperature growth rate results in a gradual increase in the air temperature of the three cooling strategies as the ventilation distance is prolonged. The difference in the wall temperature between the TN and TIL tunnels is 16.20 °C at  $L = 200$  m, which increases to 20.23 °C and 25.73 °C when the ventilation distance rises to 500 m and 1000 m, while that difference between the TIL and TIL-HE tunnels increases from 24.17 °C to 32.48 °C and 44.28 °C. That indicates that lining a TIL weakens the temperature growth, while heat exchangers further reduce the airflow temperature. Moreover, these cooling effects become increasingly effective with expanding ventilation distances, suggesting that

heat exchangers play a significant role in enhancing the airflow cooling effect to lower the construction costs of high-temperature tunnels.

### 3.3. Influence of TIL Parameters on Wall Temperature Distribution Under the TIL Strategy

#### 3.3.1. Influence of TIL Thermal Conductivity on Temperature Distribution

Figure 9a illustrates the wall temperature distribution along the ventilation direction with varying TIL thermal conductivities under the TIL strategy. The wall temperature decreases as the TIL thermal conductivity descends, presenting a decrease from 45.79 °C to 29.17 °C at  $L = 1000$  m when the TIL thermal conductivity decreases from 0.10 W/(m·K) to 0.02 W/(m·K). Moreover, the temperature reduction gradually increases with decreased TIL thermal conductivity, showing a 2.64 °C reduction in wall temperature as the thermal conductivity decreases from 0.10 W/(m·K) to 0.08 W/(m·K), which further increases to 6.28 °C when the thermal conductivity decreases from 0.04 W/(m·K) to 0.02 W/(m·K). This means that reducing the TIL thermal conductivity effectively lowers tunnel temperatures, presenting an acceptable effect for controlling airflow temperature in high-temperature tunnels by utilizing ultra-low thermal conductivity materials. However, it is important to note that the cost of lining TIL rises exponentially as thermal conductivity decreases [24,41,42]. Therefore, selecting the appropriate thermal conductivity, and balancing project costs and safety requirements, emerges as the optimal strategy in practical high-temperature engineering applications [43].

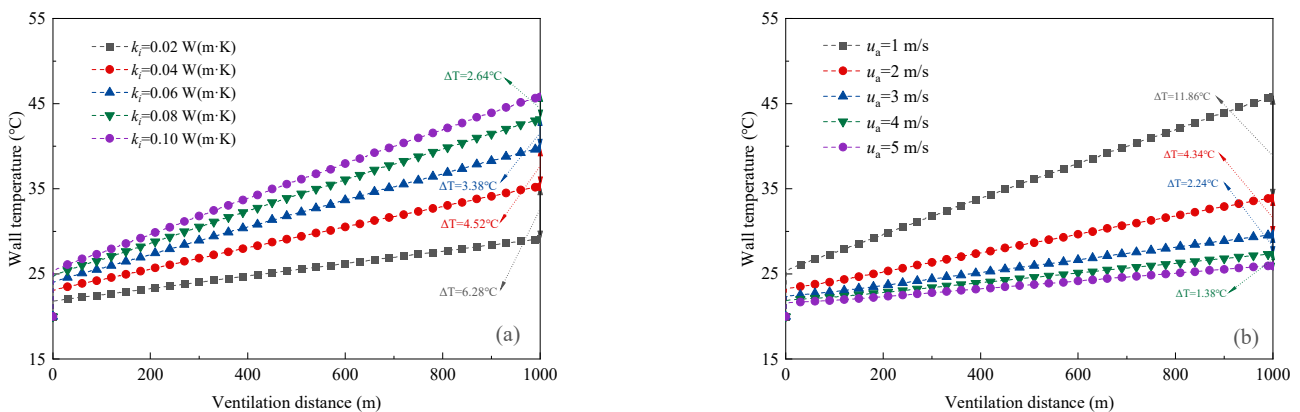


**Figure 9.** Wall temperature along ventilation direction under different TIL parameters: (a) wall temperature under different thermal conductivity and (b) wall temperature under different airflow velocity.

#### 3.3.2. Influence of Airflow Velocity on Wall Temperature Distribution

The wall temperature decreases with increasing the airflow velocity ( $u_a$ ) under the TIL strategy, which descends from 45.76 °C to 25.94 °C at  $L = 1000$  m as the airflow velocity increases from 1 m/s to 5 m/s (Figure 9b). Unlike thermal conductivity, the cooling benefits brought by increasing airflow speed rapidly decrease, significantly diminishing the cooling benefits with higher airflow speeds. Increasing the airflow velocity from 1 m/s to 2 m/s leads to a temperature drop of 11.86 °C at  $L = 1000$  m, which drops to 1.38 °C with the airflow velocity rising from 4 m/s to 5 m/s. This suggests that merely increasing airflow velocity in high-temperature tunnels, despite aligning with a TIL, is inadequate for achieving acceptable cooling effects. Rather, a shift in the cooling strategy, involving the integration of combined heat exchangers, is imperative to attain the desired outcomes.

### 3.4. Influence of HE Parameters on Wall Temperature Distribution Under the TIL-HE Strategy

#### 3.4.1. Influence of Water Flow Velocity on Wall Temperature Distribution

Figure 10a depicts the variations in wall temperature along the ventilation direction with different water flow velocities ( $u_w$ ) under the TIL-HE strategy with eight heat exchang-

ers (HEs). Increasing the water velocity from 0.2 m/s to 1.0 m/s enhances the cooling effect, decreasing the wall temperature from 27.46 °C to 24.05 °C at  $L = 1000$  m. Although the wall temperature consistently remains below 30 °C regardless of the water flow velocity, the cooling benefits derived from increasing the water flow velocity decline rapidly, similar to the diminishing returns seen with higher airflow velocities. The decrease in wall temperature is only 0.13 °C when the velocity increases from 0.8 m/s to 1.0 m/s, which equals 0.0625 times that increasing from 0.2 m/s to 0.4 m/s. Thus, further increasing the water flow velocity is unacceptable for cooling airflow temperature when the water flow velocity exceeds 0.4 m/s.

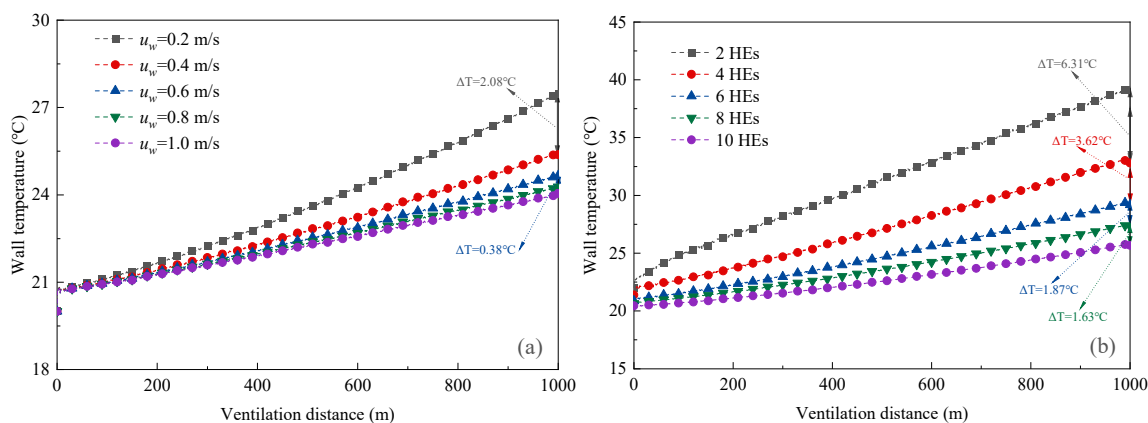


**Figure 10.** Wall temperature along the ventilation direction under different HE parameters: (a) wall temperature under different water flow velocities and (b) wall temperature under different HE number.

### 3.4.2. Influence of the Number of Heat Exchangers on Wall Temperature Distribution

The cooling benefits provided by increasing the HE number are higher than those provided by increasing water flow velocity under the TIL-HE strategy (Figure 10b). The wall temperature decreases from 39.11 °C to 25.68 °C as the HE number increases from 2 to 10. The wall temperature reduction at  $L = 1000$  m is 6.31 °C as the HE number increases from 2 to 4, which remains at 1.63 °C even as the HE number increases from 8 to 10. This is slightly higher than that seen when water flow velocity increases from 0.8 m/s to 1.0 m/s. Moreover, the wall temperature remains below 30 °C when the HE number reaches 6, presenting an acceptable cooling effect.

## 3.5. Average Airflow Temperature and Valid Ventilation Distance

### 3.5.1. Valid Ventilation Distance Under Different Cooling Strategies

The airflow temperature in a high-temperature tunnel rises incrementally with increasing ventilation distance, leading to reduced labor efficiency and potentially mandating production suspension if the air temperature surpasses the allowable threshold. Industry regulations mandate that the average airflow temperature within a tunnel must not exceed a specified limit, known as the allowable temperature, to ensure a safe and comfortable working environment. According to the Coal Mine Safety Regulation (2016) in China, this allowable temperature is 30 °C; exceeding this limit requires an immediate halt to excavation and the implementation of cooling measures. The ventilation distance at which the allowable temperature is reached is termed the valid ventilation distance (VVD). This metric provides a more intuitive representation of the evolution of airflow temperature and aids in assessing the technical challenges and associated cooling costs in high-temperature tunnels.

As shown in Figure 11, the average airflow temperature along the ventilation direction increases linearly as the ventilation distance extends from 0 m to 1000 m with different growth rates under the different cooling strategies. The highest growth rate exists in the NT tunnel, where the average temperature grows to 30 °C when the airflow reaches 232.42 m, resulting in the shortest VVD (point a in Figure 11). The VVD extends to 481.53 m (point b in Figure 11) when lining a TIL with a thermal conductivity of 0.1 W/(m·K) and a thickness of 0.25 m, presenting a VVD growth rate of 107.18%. The growth rate of airflow temperature is lowest in the TIL-HE tunnel, resulting in the VVD further increasing to over 1000 m (point c in Figure 11). This means that TIL-HE significantly outperforms TIL in decreasing airflow temperature, and employing 8 HEs is feasible under the same insulation layer and other engineering parameters.

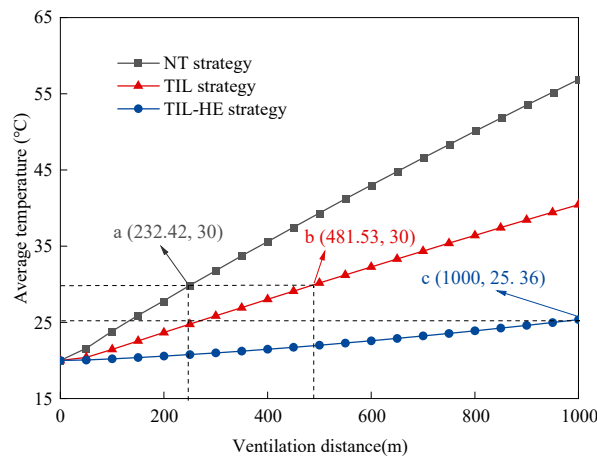


Figure 11. Average airflow temperature and VVD under different strategies.

### 3.5.2. Average Airflow Temperature Variation Under Different HE Parameters

Figure 12 presents the average airflow temperature along the ventilation direction in the high-temperature tunnel at different water flow velocities ( $u_w$ ) under the TIL-HE strategy with 8 HEs. The average airflow temperature peaks at 25.36 °C at  $u_w = 0.2$  m/s and  $L = 1000$  m, which gradually decreases as the water flow velocity increases, albeit at a diminishing rate. Specifically, the temperature difference observed between  $u_w = 0.2$  m/s and  $u_w = 0.4$  m/s is 1.37 °C, whereas that between  $u_w = 0.8$  m/s and  $u_w = 1.0$  m/s drops to merely 0.18 °C. Note that although the cooling effect of increasing the water flow velocity diminishes, the TIL-HE strategies utilizing 8 HEs can still ensure an effective ventilation distance exceeding 1000 m, irrespective of the water flow velocity.

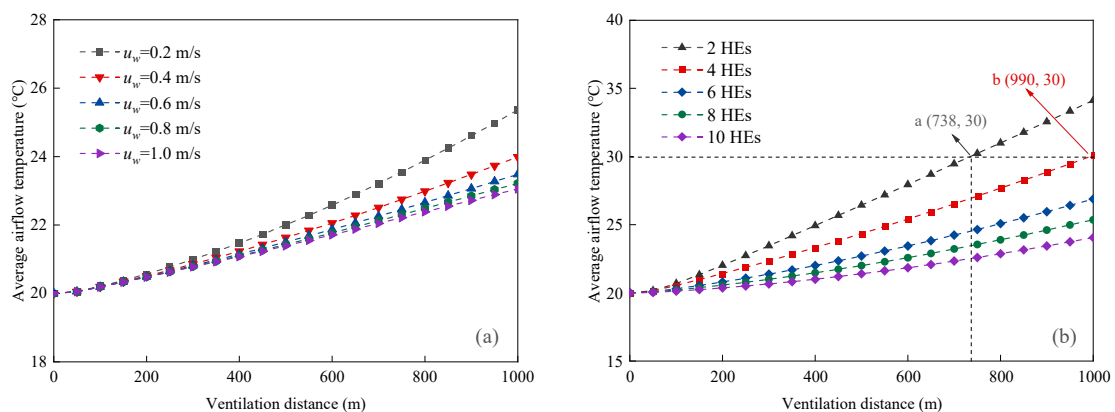


Figure 12. Variation in average airflow temperature under different HE parameters: (a) average airflow temperature under different water flow velocities and (b) average airflow temperature under different HE number.

### 3.5.3. VVD Variation Under Different HE Parameters

The tunnel length is constrained to 1000 m for the sake of computation, which presents challenges in directly determining the VVDs under various operational conditions. Thus, we employed fitting curves to calculate VVDs under different TIL-HE cooling strategies parameters. Assuming the ventilation distance is sufficiently long, the average fluid temperature will converge towards the initial temperature of the surrounding rock. There is a functional relationship between effective ventilation distance and average fluid temperature, which can be expressed as:

$$T_a = A * e^{(-x/B)} + C \tag{12}$$

where  $x$  denotes the ventilation distance, and  $A$ ,  $B$ , and  $C$  are constant variables associated with HE number and water velocity.

Figure 13 illustrates the fitted curve and its mathematical expression under different HE numbers and water velocities, indicating that the VVD increases as the HE number grows and the water velocity increases. Specifically, the VVD rises from 738.05 m to 1576.58 m as the HE number increases from 2 to 10, resulting in an overall growth rate of 113.60%. Notably, the increment in VVD induced by increasing per 2 HEs descends. For instance, when the HE number increases from 2 to 4, the VVD increases by 252.99 m, but this increment diminishes to 243.94 m when the HE number advances from 4 to 6, and further decreases to 145.15 m as the HE number rises from 8 to 10. This gradual attenuation in VVD concerning changes in parameters aligns with findings from prior studies conducted in similar environments [8], which also corroborate the variations in airflow temperature discussed in Section 3.3.

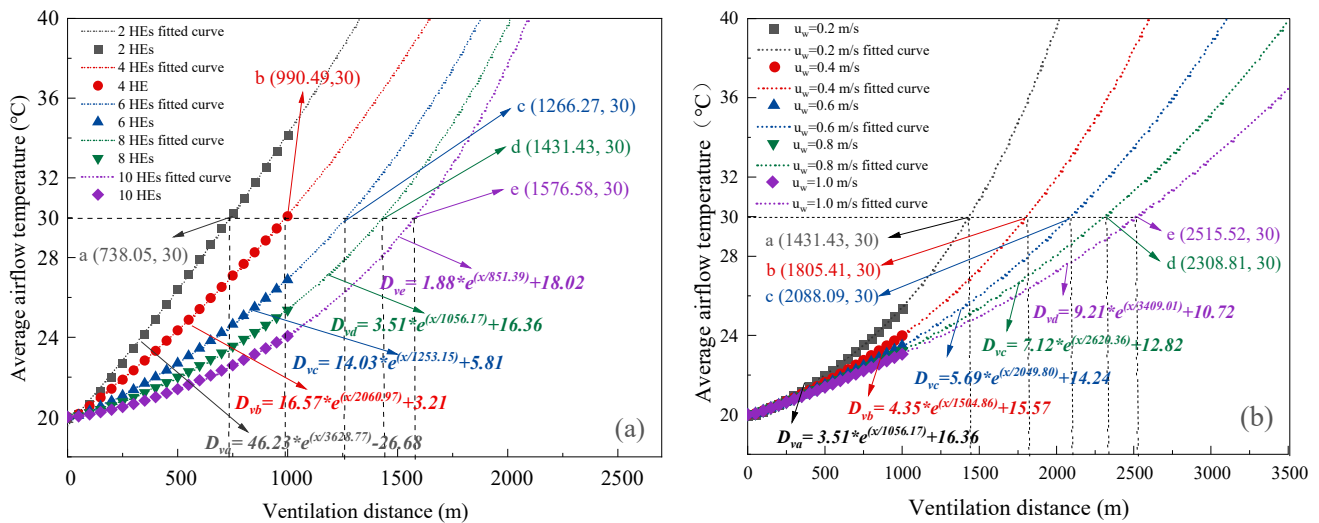


**Figure 13.** VVD variation under different HE parameters: (a) VVD under different HE number and (b) VVD under different water flow velocities.

Similarly, the VVD extends to 1431.43 m at a water velocity of 0.2 m/s, which increases to 1805.41 m, 2088.09 m, 2308.81 m, and 2515.52 m with the water velocity increasing to 0.4 m/s, 0.6 m/s, 0.8 m/s, and 1.0 m/s, presenting corresponding growth rates of 26.13%, 15.66%, 10.54%, and 8.95%, respectively. Note that the VVD increment associated with a 0.2 m/s increase in water velocity diminishes from 26.13% to 8.95%, paralleling the trend observed with varying HE numbers. Consequently, optimizing the selection of HE numbers and water velocity emerges as a critical strategy for effectively addressing the cooling requirements of tunnel projects.

### 3.5.4. VVD Variation Under Different HE Positions

We compared the average airflow temperature and the corresponding VVDs for HEs positioned within the surrounding rock and the insulation layer to evaluate the influence of HE position on cooling effectiveness (Figure 14). The VVD measures 775.23 m for HEs located within the insulation layer, which increases to 1431.43 m, corresponding to a growth rate of 84.65%. This observation indicates that embedding the HE in the surrounding rock yields the most effective cooling. This enhanced performance can be attributed to the insulation layer's role in reducing heat transfer from the surrounding rock to the tunnel air when the HE is positioned within the insulation layer. Consequently, the smaller temperature differential between the interior and exterior of the heat exchanger diminishes the heat loss transferred away by the water flow within the HEs, leading to a relatively lower cooling effect on the tunnel airflow [19,37,44].

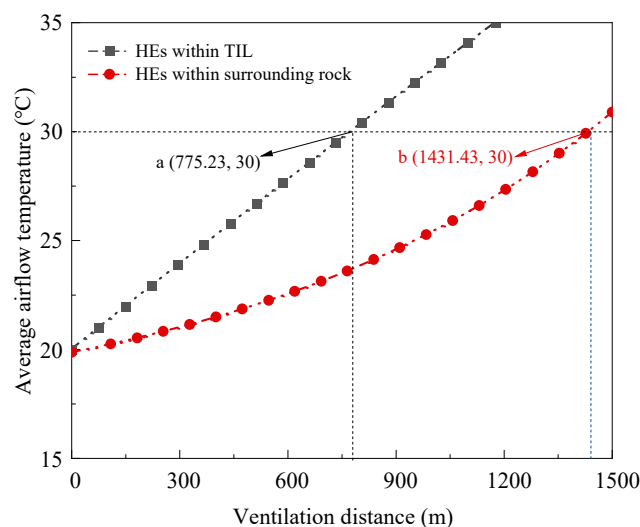


Figure 14. VVD variation of different HE positions.

## 4. Discussion

The increasing temperature in tunnel environments requires a combined cooling strategy that integrates thermal insulation layers and heat exchangers as a prerequisite for ensuring safe construction and operation [2]. The newly proposed TIL-HE strategy offers an acceptable approach to tackle such issues, as its cooling superiority was verified by comparing tunnel airflow temperature and VVD against two other strategies.

While integrated cooling strategies demonstrate high performance, they also result in significant engineering costs due to complex construction involving multiple boreholes for heat exchanger installation. Our longitudinal arrangement of heat exchangers reduces construction challenges and project loads compared to traditional radial drilling methods, thereby lowering tunnel construction costs.

However, comparisons between the proposed cooling strategy and other combined approaches have not yet been conducted. Additionally, whether the outlet water flow temperature meets the threshold for geothermal energy utilization remains unexplored, which will be a focus of future research.

## 5. Conclusions

In this paper, we proposed a cooling strategy that integrates insulating layers and heat exchangers along the tunnel direction, and its cooling superiority was verified by comparing airflow temperature and vertical VVD against two other cooling strategies. The main conclusions are as follows:

- (1) The TIL-HE demonstrates enhanced performance in cooling airflow temperature within high-temperature tunnels, leading to a marked reduction in average airflow temperature relative to the NT and TIL strategies. It yields an increase in VVD by 830.61 m, representing a 172.49% improvement compared to the TIL strategy.
- (2) Increasing water flow velocity and the HE number enhance cooling effectiveness, showing a reduction in the airflow temperature and growth in the VVD. Specifically, the VVD extends from 1312.14 m to 2388.9 m as the water velocity escalates from 0.2 m/s to 1.0 m/s, while it grows from 738.00 m to 1576.58 m as the HE number increases from 2 to 10.
- (3) Building heat exchangers within the surrounding rock yields superior cooling effects, outperforming configurations where exchangers are situated within insulation layers or cement layers. Notably, the VVD under the surrounding rock layout increases by 656.20 m with a rate of 84.65% compared to the insulation layout.

**Author Contributions:** Conceptualization, F.K.; methodology, F.K. and J.C.; software, F.K. and W.Z.; validation, W.Z. and R.C.; formal analysis, B.Q.; investigation, R.C.; resources, J.M.; data curation, Z.Y.; writing—original draft preparation, F.K. and J.C.; writing—review and editing, F.K., B.Q. and G.S.; visualization, R.C.; supervision, F.K. and G.S.; project administration, F.K.; funding acquisition, F.K. and B.Q. All authors have read and agreed to the published version of the manuscript.

**Funding:** This research was funded by the National Natural Science Foundation of China (52179097), the Projects of Talents Recruitment of GDUPT (XJ2022000801, 2023rcyj2022), the Higher Education Special Project of Guangdong Provincial Education Research (2024361), and the Project of Guangdong Provincial Higher Education Institute (24GYB45).

**Institutional Review Board Statement:** Not applicable.

**Informed Consent Statement:** Informed consent was obtained from all subjects involved in the study.

**Data Availability Statement:** The original contributions presented in this study are included in the article. Further inquiries can be directed to the corresponding authors.

**Conflicts of Interest:** The authors declare no conflicts of interest.

## References

1. Yuanming, L.; Xuefu, Z.; Wenbing, Y.; Shujuan, Z.; Zhiqiang, L.; Jianzhang, X. Three-dimensional nonlinear analysis for the coupled problem of the heat transfer of the surrounding rock and the heat convection between the air and the surrounding rock in cold-region tunnel. *Tunn. Undergr. Space Technol.* **2005**, *20*, 323–332. [[CrossRef](#)]
2. Che, J.; Li, A.; Guo, J.; Ma, Y.; Li, J.; Yang, C.; Che, L. Theoretical and experimental investigation on the thermal penetration depth in the surrounding rock of a deeply buried high-temperature tunnel. *Int. J. Therm. Sci.* **2024**, *198*, 108876. [[CrossRef](#)]
3. Deng, L.-C.; Li, X.-Z.; Wang, Y.-C.; Wu, Y.; Huang, Z.; Jiang, C. Effect of Temperature on Macroscopic and Microscopic Properties of Sandstone From Qidong Coal Mine. *Rock. Mech. Rock. Eng.* **2022**, *55*, 71–90. [[CrossRef](#)]
4. Lin, M.; Zhou, P.; Jiang, Y.; Zhou, F.; Lin, J.; Wang, Z. Numerical investigation on comprehensive control system of cooling and heat insulation for high geothermal tunnel: A case study on the highway tunnel with the highest temperature in China. *Int. J. Therm. Sci.* **2022**, *173*, 107385. [[CrossRef](#)]
5. Zhu, H.; Yan, J.; Liang, W. Challenges and Development Prospects of Ultra-Long and Ultra-Deep Mountain Tunnels. *Engineering* **2019**, *5*, 384–392. [[CrossRef](#)]
6. Liu, S.; Fu, J.; Yang, J.; Feng, H. Numerical Simulation of Temperature Effects on Mechanical Behavior of the Railway Tunnel in Tibet. *KSCE J. Civ. Eng.* **2020**, *24*, 3875–3883. [[CrossRef](#)]
7. Kang, F.; Li, Y.; Tang, C.; Li, T.; Wang, K. Numerical Study on Thermal Damage Behavior and Heat Insulation Protection in a High-Temperature Tunnel. *Appl. Sci.* **2021**, *11*, 7010. [[CrossRef](#)]
8. Kang, F.; Li, Y.; Tang, C. Numerical study on airflow temperature field in a high-temperature tunnel with insulation layer. *Appl. Therm. Eng.* **2020**, *179*, 115654. [[CrossRef](#)]
9. Zhao, J.; Tang, C.A.; Wang, S.J. Excavation based enhanced geothermal system (EGS-E): Introduction to a new concept. *Geomech. Geophys. Geo* **2020**, *6*, 6. [[CrossRef](#)]

10. Chen, B.; Li, Y.; Tang, C. Numerical Study on the Zonal Disintegration of a Deeply Buried High-Temperature Roadway during Cooling. *Comput. Geotech.* **2024**, *165*, 105848. [[CrossRef](#)]
11. Zhou, P.; Feng, Y.; Zhou, F.; Wei, Z.; Gou, S.; Xu, H.; Wang, Z. Evaluation system of worker comfort for high geothermal tunnel during construction: A case study on the highway tunnel with the highest temperature in China. *Tunn. Undergr. Space Technol.* **2023**, *135*, 105028. [[CrossRef](#)]
12. Zhang, H.; Hao, Z.; Zhang, G.; Tao, Y.; Wang, L. The cooling effect of high geothermal tunnel construction environment: A case of ice and spray method in an extra-long tunnel. *Int. J. Therm. Sci.* **2022**, *178*, 107606. [[CrossRef](#)]
13. Han, Q.; Zhang, Y.; Kongqing, L.; Shenghua, Z. Computational evaluation of cooling system under deep hot and humid coal mine in China: A thermal comfort study. *Tunn. Undergr. Space Technol.* **2019**, *90*, 394–403. [[CrossRef](#)]
14. Chen, X.; Zhou, X.; Zhong, Z.; Liang, N.; Wang, Y.; Zhang, X. Study on temperature field and influencing factors of the high geothermal tunnel with extra-long one-end construction ventilation. *Int. J. Therm. Sci.* **2023**, *191*, 108322. [[CrossRef](#)]
15. Guo, P.; He, M.; Zheng, L.; Zhang, N. A geothermal recycling system for cooling and heating in deep mines. *Appl. Therm. Eng.* **2017**, *116*, 833–839. [[CrossRef](#)]
16. Wang, H. Numerical study of surrounding rock heat dissipation and wind temperature prediction in high geotemperature coal face. *Energy Explor. Exploit.* **2024**, *42*, 17–39. [[CrossRef](#)]
17. Liu, R.; Jiang, D.; He, Y.; Zhang, H.; Chen, J.; Ren, S.; Zhou, Z. Study on cooling measures and ventilation cooling device of high ground temperature tunnel. *J. Therm. Anal. Calorim.* **2024**, *149*, 3347–3365. [[CrossRef](#)]
18. Chen, L.; Zhao, J.; Meng, X.; Liu, Z.; Liu, G. Experimental evaluation on mechanical and thermal insulation properties of shotcrete under constant-variable temperature. *Struct. Concr.* **2023**, *24*, 2041–2056. [[CrossRef](#)]
19. Zhang, K.; Ren, J.; Du, W.; Luo, L.; Liu, J.; Deng, S. Thermal insulation performance and dynamic response of anti-freeze subgrade of high-speed railway in seasonally frozen regions. *Transp. Geotech.* **2023**, *42*, 101081. [[CrossRef](#)]
20. Ma, Q.; Luo, X.; Lai, Y.; Niu, F.; Gao, J. Numerical investigation on thermal insulation layer of a tunnel in seasonally frozen regions. *Appl. Therm. Eng.* **2018**, *138*, 280–291. [[CrossRef](#)]
21. Luo, M.-R.; Zhang, X.-Y.; Yuan, Z.; Wu, X.; Zeng, Y.-H.; Ye, Y.-Z. Thermal performance comparison and new layout scheme study of high geothermal tunnel insulation layer. *Case Stud. Therm. Eng.* **2023**, *52*, 103780. [[CrossRef](#)]
22. Han, F.; Liu, Z.; Li, J.; Yu, W.; Yan, Q.; Zhou, Y.; Zhang, S.; Chen, L. Prediction of thermal conductivities of insulation materials under water immersion and freeze–thaw conditions for tunnels in cold regions. *Tunn. Undergr. Space Technol.* **2024**, *144*, 105531. [[CrossRef](#)]
23. Al-Homoud, M.S. Performance characteristics and practical applications of common building thermal insulation materials. *Build. Environ.* **2005**, *40*, 353–366. [[CrossRef](#)]
24. Li, Z.; Zhao, J.; Liu, T.; Liu, L. Study on Radial and Longitudinal Zoning of Insulation Layer in Alpine Tunnel under Wind Field. *Sustainability* **2023**, *15*, 6010. [[CrossRef](#)]
25. Wang, L.; Zhang, C.; Cui, G.; Wang, X.; Ye, Z. Study on the performance of the new composite thermal insulation lining for the railway operational tunnel in cold regions. *Case Stud. Therm. Eng.* **2022**, *36*, 102098. [[CrossRef](#)]
26. Cui, G.; Ma, J.; Wang, L.; Wang, X.; Wang, D. A new off-wall insulation liner for high-speed railway tunnels in cold regions. *Case Stud. Therm. Eng.* **2021**, *28*, 101652. [[CrossRef](#)]
27. Li, C.; Zhang, G.; Xiao, S.; Shi, Y.; Xu, C.; Sun, Y. Numerical investigation on thermal performance enhancement mechanism of tunnel lining GHEs using two-phase closed thermosyphons for building cooling. *Renew. Energy* **2023**, *212*, 875–886. [[CrossRef](#)]
28. Zhang, Y.; Xia, C.; Zhou, S.; Cao, S. A novel sustainable cooling system in a tunnel with high geotemperature: Concept and thermal performance. *Tunn. Undergr. Space Technol.* **2023**, *137*, 105122. [[CrossRef](#)]
29. Ma, Y.; Xu, L.; Shi, X. The multi-factor influence of frost resistance and prevention effect of tunnel thermal insulation layer in cold areas. *Alex. Eng. J.* **2023**, *78*, 15–25. [[CrossRef](#)]
30. Wang, Y.; Zhou, X.; Liu, X.; Chen, X.; Xu, Q.; Wang, Q. Ambient temperature prediction model and cooling requirement analyze in the high-altitude construction tunnel passing through the abnormally high geothermal region. *Tunn. Undergr. Space Technol.* **2023**, *141*, 105360. [[CrossRef](#)]
31. Tan, X.; Chen, W.; Yang, D.; Dai, Y.; Wu, G.; Yang, J.; Yu, H.; Tian, H.; Zhao, W. Study on the influence of airflow on the temperature of the surrounding rock in a cold region tunnel and its application to insulation layer design. *Appl. Therm. Eng.* **2014**, *67*, 320–334. [[CrossRef](#)]
32. Balabel, A.; El-Askary, W.A. On the performance of linear and nonlinear turbulence models in various jet flow applications. *Eur. J. Mech. B Fluids* **2011**, *30*, 325–340. [[CrossRef](#)]
33. Launder, B.E. Current capabilities for modelling turbulence in industrial flows. *Appl. Sci. Res.* **1991**, *48*, 247–269. [[CrossRef](#)]
34. Insana, A.; Barla, M. Experimental and numerical investigations on the energy performance of a thermo-active tunnel. *Renew. Energy* **2020**, *152*, 781–792. [[CrossRef](#)]

35. Nematchoua, M.K.; Raminosoa, C.R.R.; Mamiharijaona, R.; Rene, T.; Orosa, J.A.; Elvis, W.; Meukam, P. Study of the economical and optimum thermal insulation thickness for buildings in a wet and hot tropical climate: Case of Cameroon. *Renew. Sustain. Energy Rev.* **2015**, *50*, 1192–1202. [[CrossRef](#)]
36. COMSOL Co., Ltd. COMSOL Documentation for Version 6.0. Available online: <https://doc.comsol.com/> (accessed on 17 December 2024).
37. Jia, H.; Zou, Q.; Cui, B.; Zeng, J. Thermal Insulation Properties and Simulation Analysis of Foam Concrete Regulated by Mechanical and Chemical Foaming. *ACS Omega* **2023**, *8*, 48091–48103. [[CrossRef](#)]
38. Hu, S.; Cai, Y.; Zhang, L.; Yan, Z.; Pang, S. Numerical Simulation of Rock Breaking by High-Temperature and High-Pressure Water under Thermal Driving. *Geofluids* **2022**, *2022*, 5005256. [[CrossRef](#)]
39. Tan, X.; Chen, W.; Yu, H.; Liu, D. Study of temperature field of tunnel surrounding rock in cold regions considering effect of ventilation and length design of insulation material. *Yanshilixue Yu Gongcheng Xuebao/Chin. J. Rock. Mech. Eng.* **2013**, *32*, 1400–1409.
40. Blay, D.; Mergui, S.; Niculae, C. Confined turbulent mixed convection in the presence of a horizontal buoyant wall jet. *Fundam. Mix. Convect.* **1992**, *213*, 65–72.
41. Bahadori, A.; Vuthaluru, H.B. A simple correlation for estimation of economic thickness of thermal insulation for process piping and equipment. *Appl. Therm. Eng.* **2010**, *30*, 254–259. [[CrossRef](#)]
42. Daouas, N.; Hassen, Z.; Aissia, H.B. Analytical periodic solution for the study of thermal performance and optimum insulation thickness of building walls in Tunisia. *Appl. Therm. Eng.* **2010**, *30*, 319–326. [[CrossRef](#)]
43. Li, Y.; Sun, Y.; Zhuang, Y.; Duan, L.; Xie, K. Thermal Conductivity Characteristics of Thermal Insulation Materials Immersed in Water for Cold-Region Tunnels. *Adv. Mater. Sci. Eng.* **2020**, *2020*, 9345615. [[CrossRef](#)]
44. Rosti, B.; Omidvar, A.; Monghasemi, N. Optimum position and distribution of insulation layers for exterior walls of a building conditioned by earth-air heat exchanger. *Appl. Therm. Eng.* **2019**, *163*, 114362. [[CrossRef](#)]

**Disclaimer/Publisher’s Note:** The statements, opinions and data contained in all publications are solely those of the individual author(s) and contributor(s) and not of MDPI and/or the editor(s). MDPI and/or the editor(s) disclaim responsibility for any injury to people or property resulting from any ideas, methods, instructions or products referred to in the content.